

Determination of a Correlation of Sunspot Number and 20.1 MHz Solar Radio Bursts

J.A. Burlison

Advisor: Dr. Chuck Higgins

Department of Physics and Astronomy

Middle Tennessee State University

Murfreesboro, Tennessee 31732

May 07, 2010

ABSTRACT

There are many phenomena about the Sun that scientists have yet to fully understand. Some of these questions involve the sun's magnetic field, sunspots, solar flares, and solar radio bursts. We know that due to differential rotation the magnetic fields get tangled and twisted resulting in sunspots. It is theorized that solar radio bursts are a result of solar flares accelerating charged particles in the magnetic field. These accelerated particles emit a wide variety of frequencies. Using a two dipole antenna and a Radio JOVE receiver kit, we obtained over two years of solar burst data at 20.1 MHz. Using these data, a graph was created comparing the visual sunspot number and 20.1 MHz solar burst data. Comparing this to 10.7 cm solar flux data, which is a result of the synchrotron mechanism, the cyclic nature seems identical. We then plotted the sunspot number versus 20.1 MHz radio bursts and found the coefficient of correlation to be 0.65. From this experimental result as well as the theory, we show that there is a relationship between sunspots and solar radio bursts.

I. Background and Introduction

This paper presents a strong relationship between the sunspot number and the number of low frequency solar radio bursts. The data used was from our own antenna in Murfreesboro Tennessee as well those of as Jim Brown in Beaver Pennsylvania and Jim Theiman from NASA Goddard in Greenbelt Maryland. Using this data, graphs of the number of solar radio bursts alongside sunspot number versus time were created. Based on what we know of the physics behind sunspots and solar bursts, the data agrees with the theory to a considerable degree. Based on this result we expect the solar burst number to increase as more sunspots are seen.

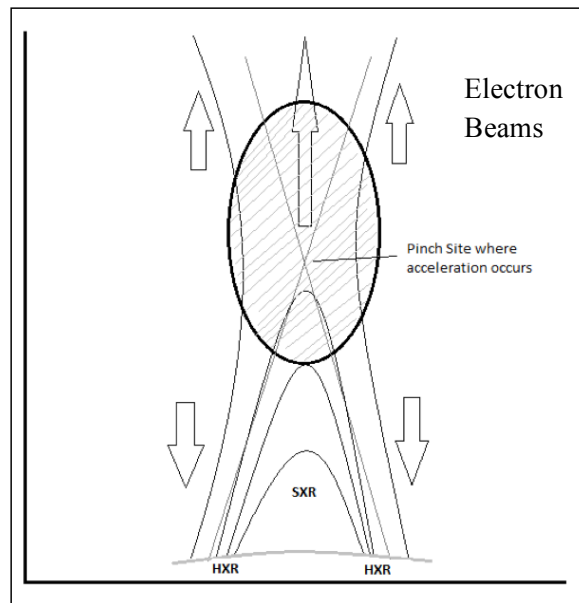


Figure 1: Diagram of a reconnection point (adopted from Fig. 2.7, Gary, Keller: 2004)

Astronomers now realize that the Sun's magnetic field is directly responsible for sunspots and other solar phenomena like prominences, flares, and their resulting coronal mass ejections (CME's). These eruptive events spew particles and radiation into space, which are received by radio antennas. Solar bursts are a result of plasma (gas of charged particles) being trapped in the

tangling of magnetic field lines (Gary, Keller; 2004). A plasma cloud is pinched off as the magnetic fields reconnect, sending the cloud into space as thermal energy at a considerable fraction of the speed of light as shown in Figure 1, where HXR represents hard (most energetic x-rays, SXR represents soft x-rays (least energetic), and the arrows represent the direction of the electron beams. The upward electron beams generally result in the Type III solar bursts we receive with radio antennas (Gary, Keller; 2004).

The temperature around a solar burst can be millions of Kelvin, and the output of a solar flare releases about 10^{14} Joules from the intense magnetic field around a sunspot. CME's are even greater in energy output than flares and can eject gas at hundreds of kilometers per second. It is believed that CME's are a result of drastic changes in the solar magnetic field, and astronomers have found that solar bursts occur in areas of complex sunspot groups (Freedman, Kaufmann; 2005). Our research asks whether a correlation exists between the number of solar radio bursts and number of visible sunspots.

Sunspots are produced by magnetic twisting, which occurs due to differential rotation, as shown by the Babcock Magnetic Dynamo. As the magnetic fields get more and more twisted, more tangles and kinks occur, which protrude from the surface of the sun. These protrusions are the sites where sunspots occur, causing the plasma to travel along the protrusions which causes the solar surface to become cooler and darker in this region (Gary, Keller; 2004). Solar bursts occur when these magnetic protrusions twist and reconnect, as illustrated in Figure 2, emitting frequencies all across the electromagnetic spectrum.

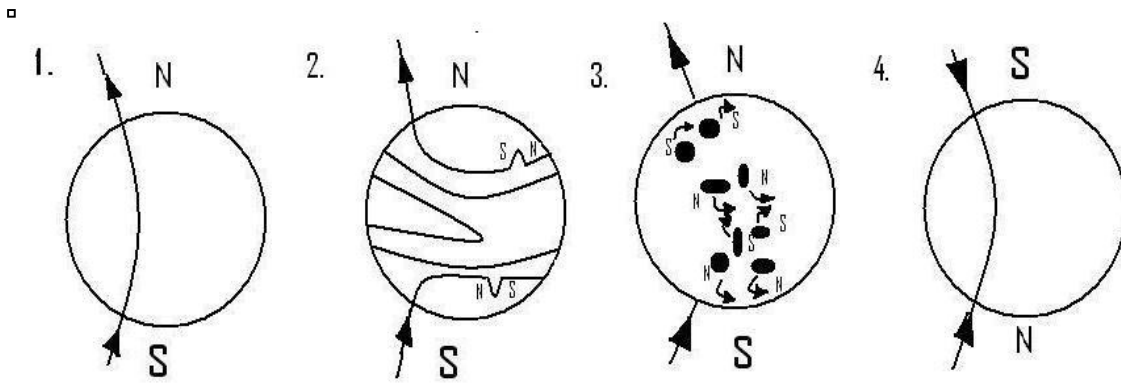


Fig. 2. Babcock Magnetic Dynamo Model (adopted from Figure 18-24, Freedman, and Kaufmann; 2005).

The first picture in Figure 2 shows the beginning of the cycle where differential rotation has had little effect on the magnetic fields; the second picture shows the result of differential rotation after many rotations; the third image shows the sunspots, each having its own poles, which are a result of the kinks; the last image shows the cycle progressing the sunspots migrate toward the equator where their mini-poles switch the overall polarity of magnetic field of the Sun.

II. Theory

The observation and study of solar bursts at a frequency of 20.1 MHz corresponds to a wavelength of about 15 meters, which lies in the radio portion of the electromagnetic spectrum. The main location of solar radio wave sources are in the corona. When charged particles are under the influence of magnetic fields, they accelerate in a helical pattern, and exhibit periodic behavior, resulting in cyclotron or synchrotron radiation patterns. Let us consider the difference between cyclotron and synchrotron radiation, and a short description of magnetic reconnection.

II.a Cyclotron and Synchrotron Radiation

Consider a particle moving in an electromagnetic field. The total force it would experience is shown by the Lorentz force equation, in Gaussian units:

$$\mathbf{F} = q \left[\mathbf{E} + \left(\frac{\mathbf{v}}{c} \times \mathbf{B} \right) \right], \quad (1)$$

where the contribution due to the magnetic field is:

$$\mathbf{F}_B = q \frac{\mathbf{v}}{c} \times \mathbf{B}, \quad (2)$$

which is perpendicular to both \mathbf{v} and \mathbf{B} . Relative to \mathbf{B} , the velocity can be broken down into its translational (\mathbf{v}_\parallel) and rotational (\mathbf{v}_\perp) components (Figure 3), for which the latter is:

$$v_\perp = v \sin \theta. \quad (3)$$

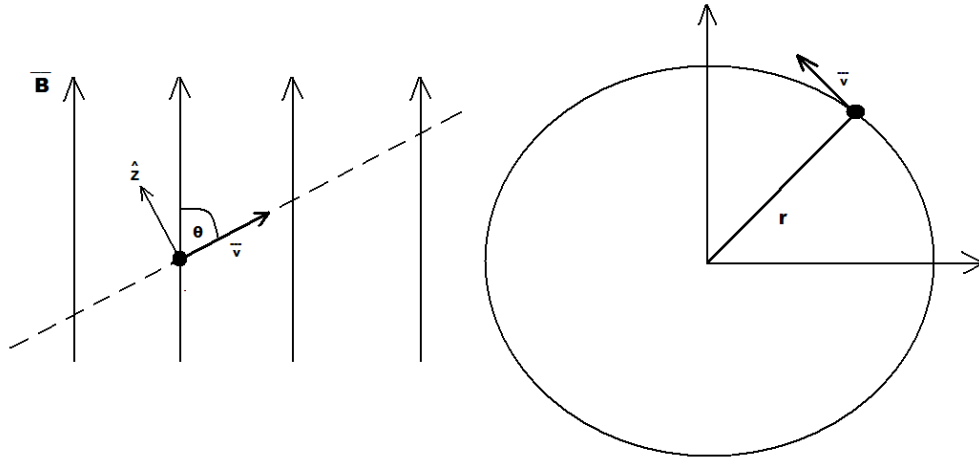


Fig. 3. Particle moving with velocity v at angle θ with respect to the magnetic field \mathbf{B} .

Thus we can see that the constantly accelerating particle emits radiation. For an electron, the equation of motion is:

$$m_e \mathbf{a} = -\frac{e}{c} \mathbf{v} \times \mathbf{B} \quad (4)$$

which becomes

$$m_e \frac{v_{\perp}^2}{r} = \left| -\frac{ev_{\perp}B}{c} \right| = \left| -\frac{evB}{c} \sin\theta \right|, \quad (5)$$

where r denotes the radius of the electron's cyclic path. From this we can define a cyclotron frequency ω_{cycl} according to

$$\omega_{cycl} = \frac{v \sin\theta}{r} \quad (6)$$

which can also be determined in terms of the magnetic field by combining Eqs. (5) and (6), which yields:

$$\omega_{cycl} \equiv \frac{eB}{m_e c} = 1.8 \times 10^7 \left(\frac{B}{1 \text{ gauss}} \right), \quad (7)$$

in which the only variable is the magnetic field. We can determine the power emitted from the accelerated charge by using the Larmor formula (Jackson) with the acceleration $|\mathbf{a}| = v_{\perp} \omega_{cycl}$:

$$P_{cycl} = \frac{2}{3} \frac{e^2}{c^3} \omega_{cycl}^2 v^2 \sin^2 \theta^2 = \frac{2}{3} \frac{e^2}{c^3} \omega_{cycl}^2 v_{\perp}^2. \quad (8)$$

It is important to note that the path travelled by the particle is circular in the v_{\parallel} frame, leading to monochromatic radiation. The frequency is also isotropic due to the fixed dipole pattern. Figure 4 illustrates the angular distribution of the radiation, the so-called cyclotron radiation, emitted by the particle.

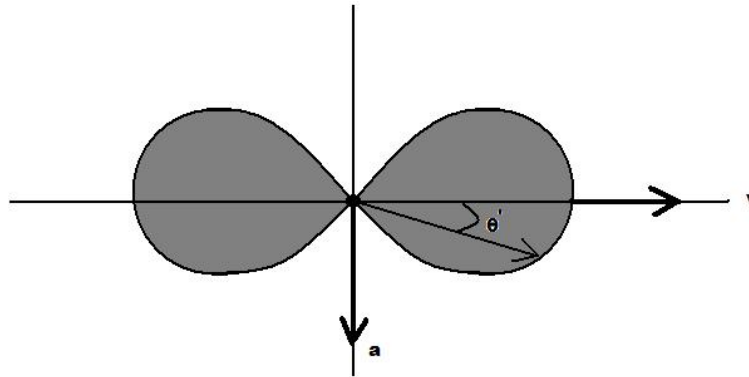


Fig.4. Angular distribution of the radiation without relativistic corrections.

As we analyze and evaluate this expression, we see that as the magnetic field gets very strong equation (8) becomes inaccurate, because for an electron travelling with a speed $v \rightarrow c$ the effects of time dilation and length contraction can no longer be neglected. The electron path will no longer be circular and will therefore emit a band of frequencies instead of just one. Also, instead of having a symmetric dipole pattern as seen in Figure (4), the radiation pattern is

extended in the direction of motion as a result of Doppler blueshifting. These changes from Figure 4 are illustrated in Figure 5.

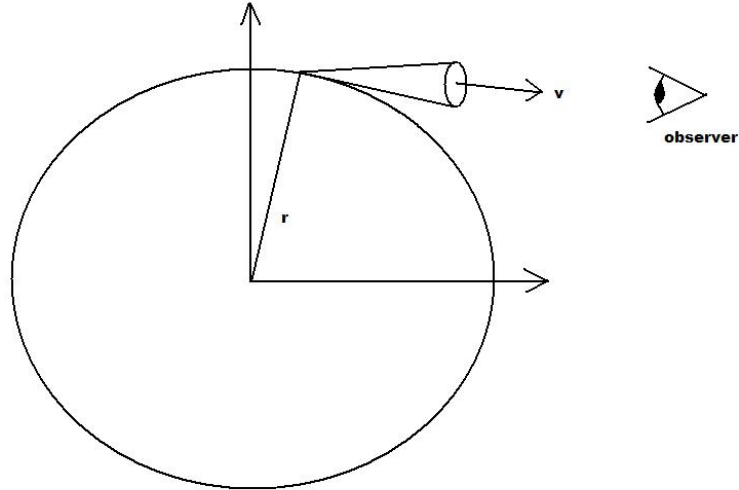


Fig. 5. Illustration of the radiation beam as a result of the relativistic dilation.

The equations of motion for the particle must change as well, to include relativistic kinematics:

$$\mathbf{F}_B = \frac{d}{dt}(\gamma m_e \mathbf{v}) = q \frac{\mathbf{v}}{c} \times \mathbf{B} \quad (9)$$

and

$$\mathbf{F}_E = \frac{d}{dt}(\gamma m_e c^2) = q \mathbf{v} \cdot \mathbf{E} = 0 \quad (10)$$

where $\gamma \equiv (1 - \frac{v^2}{c^2})^{-1/2}$. This changes the magnetic force equation to become:

$$\mathbf{F}_B = \gamma m_e \frac{d}{dt}(\mathbf{v}) = q \frac{\mathbf{v}}{c} \times \mathbf{B}. \quad (11)$$

From this we see that the acceleration is all in the perpendicular component:

$$\frac{d}{dt}(v_{||}) = 0, \quad \frac{d}{dt}(v_{\perp}) = \frac{q}{\gamma m_e c} \mathbf{v}_{\perp} \times \mathbf{B}. \quad (12)$$

Using the same steps that led us to the cyclotron frequency, we now obtain the synchrotron frequency:

$$\omega_{synch} \equiv \left| \frac{eB}{\gamma m_e c} \right|. \quad (13)$$

From the Larmor equation we get power emitted by the synchrotron radiation:

$$P_{synch} = \frac{2}{3} \frac{e^2}{c^3} \gamma^4 \frac{e^2 B^2}{\gamma^2 m_e^2 c^2} v^2 \sin^2 \theta^2 = \frac{2}{3} \frac{e^2}{c^3} \gamma^2 \omega_{synch}^2 v_{\perp}^2. \quad (14)$$

Its radiation pattern, as seen from the laboratory frame, is illustrated in Figure 6.

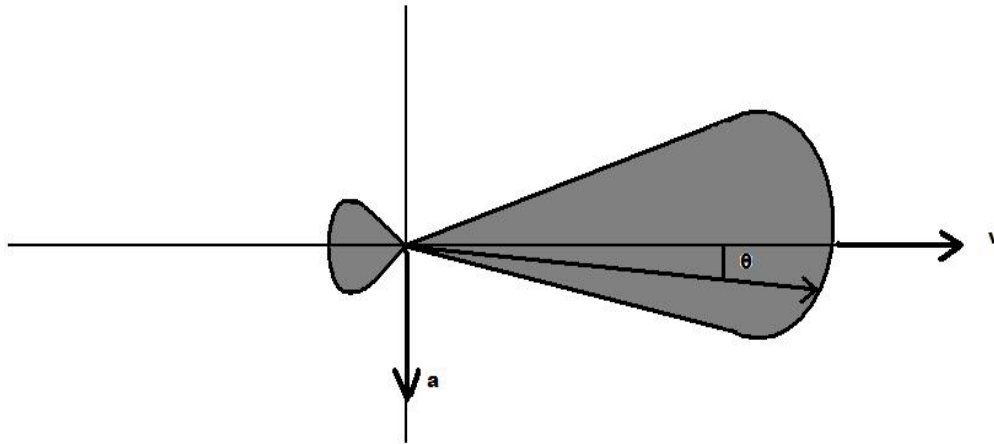


Fig. 6. Example of the radiation pattern of Fig. 5 being extended in the direction of motion.

II.b Magnetic Reconnection

In order to understand what happens during magnetic reconnection, we need to know the behavior of the magnetic field. An electric current flowing along a surface forms a *current sheet*. It is the behavior of the magnetic field interacting with the current sheet that can result in magnetic reconnection.

From Faraday's Law relate the electric field to a magnetic field that changes with time:

$$\nabla \times \mathbf{E} = -\frac{\partial \mathbf{B}}{\partial t}. \quad (15)$$

In order to have a relationship with the *total* current density, \mathbf{J} , we use Ampere's Law:

$$\nabla \times \mathbf{B} = \mu_0 \mathbf{J}. \quad (16)$$

Ohm's Law states

$$\mathbf{J} = \sigma \mathbf{E} = \sigma(\mathbf{v} \times \mathbf{B}) \quad (17)$$

where $\mathbf{E} = \sigma(\mathbf{v} \times \mathbf{B})$ results from the Lorentz transformation and \mathbf{v} denotes the relative velocity of the particles. Connecting these relations through Ohm's Law, we can rewrite the electric field as:

$$\mathbf{E} = (\mathbf{v} \times \mathbf{B}) = \frac{\mathbf{J}}{\sigma} = \frac{1}{\sigma \mu_0} (\nabla \times \mathbf{B}). \quad (18)$$

By virtue of (18) we can rewrite (15) in two different ways:

$$\frac{\partial \mathbf{B}}{\partial t} = -\nabla \times (\mathbf{v} \times \mathbf{B}) \quad (19)$$

and

$$\frac{\partial \mathbf{B}}{\partial t} = -\left[\nabla \times \frac{1}{\sigma \mu_0} (\nabla \times \mathbf{B}) \right]. \quad (20)$$

From the curl of the curl vector identity,

$$\frac{1}{\sigma \mu_0} [\nabla \times (\nabla \times \mathbf{B})] = \frac{1}{\sigma \mu_0} \nabla(\nabla \cdot \mathbf{B}) - \frac{1}{\sigma \mu_0} \nabla^2 \mathbf{B} \quad (21)$$

and noting that Gauss's Law for magnetism states that $\nabla \cdot \mathbf{B} = 0$, the first term in Eq. (20) vanishes. Now Eq. (20) may be written

$$\frac{\partial \mathbf{B}}{\partial t} = \eta \nabla^2 \mathbf{B} \quad (22)$$

where $\eta \equiv \frac{1}{\sigma \mu_0}$. In Eq (19), $\nabla \times (\mathbf{v} \times \mathbf{B})$ is known as the *advective term*, which describes how well the particles are attached to the magnetic field. In Eq. (22) $\eta \nabla^2 \mathbf{B}$ is known as the *diffusive term*, which describes how the particles will spread over time. In the case where particles are strongly attached to magnetic field, Faraday's law is best written with the advective term as in Eq. (19). If the diffusive term dominates the the particles will spread out over time, thus decreasing the current density and thinning the current sheet, in which case Faraday's Law is best written in the form of Eq. (22). An example of this latter case occurs when two fields of opposite orientation begin to diffuse toward one another and connect, as illustrated in Figure 7.

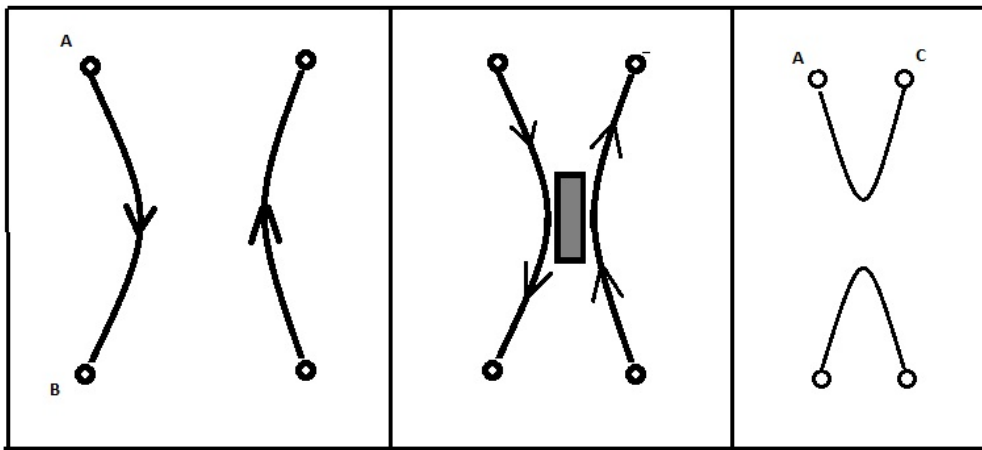


Fig. 7. Illustration of two oppositely oriented magnetic fields diffusing together and causing reconnection.

As the sun rotates, the magnetic field lines get twisted and begin to overlap each other. This twisting and overlapping creates kinks in the magnetic field lines (imagine a kink in a garden hose). This kink protrudes out of the solar surface and creates a concentrated area of intense magnetization. These magnetic kinks push away plasma from the surface, leaving a dark, cooler area on the surface (Gary, Keller; 2004). This is the cause of sunspots. As the sun continues to rotate, the field lines get more and more twisted, eventually crossing over one another. This causes the fields to change their patterns to break and reconnect. This breaking causes the electrons and other charged particles that were trapped in the field line to be released. When reconnection happens, a tremendous amount of energy is released, heating up the plasma and causing the cloud to emit radiation at synchrotron frequencies. Figure 1 shows an example of an accelerated plasma cloud resulting from a reconnection point of two magnetic field lines. All this is worked out formally in resistive magnetohydrodynamic instability theory (Priest, Forbes; 2006).

In Figure 1, the crossing of magnetic field lines defines the region where the energy is released, causing particles in the cloud to accelerate. The data that is received from a radio telescope comes from this cloud being accelerated during this process. As the cloud accelerates away from the sun, it begins to spread out and cool, giving the temperature versus time curves of the solar bursts their shape as seen in Figure 8, a typical Type III solar burst with intensity (in K) plotted as a function of Universal Time (UT). This type of solar burst is characterized by its tremendous energy released over a relatively short time (few minutes).

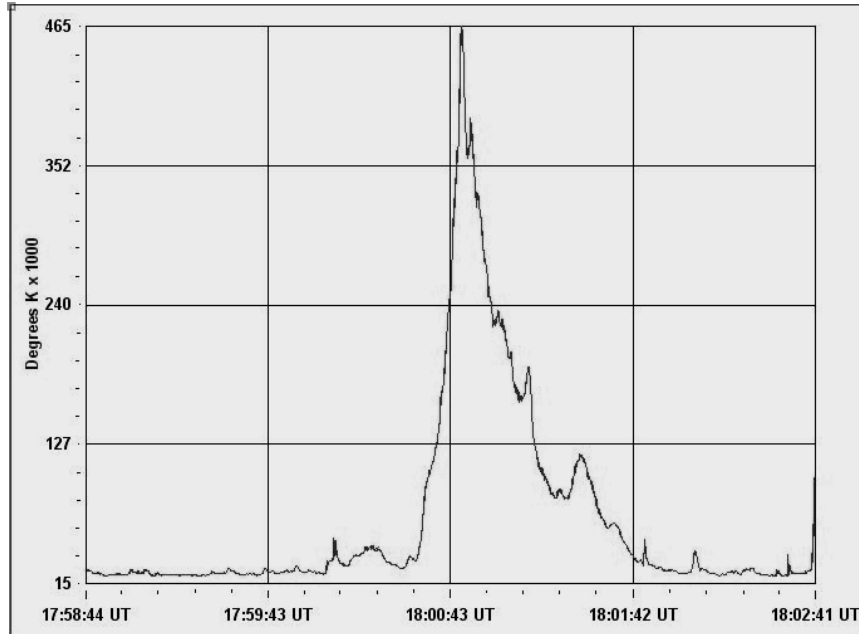


Fig. 8. Standard characteristic shape of 20.1 MHz solar radio burst.

From Figure 8 we can see that the initial burst is very sharp and the temperature rises many thousands of Kelvins. This is when the magnetic fields break and release an immense amount of energy and the plasma cloud into space. As the cloud travels, it becomes more oblate with time, spreading out and decreasing in intensity. This decreases the temperature of the cloud, which is what we see after the solar burst peak.

III. Experiment

The experimental apparatus includes a half-wave dipole antenna, a coaxial cable, and a 20 MHz Radio JOVE receiver connected to a computer with Radio-Skypipe software to display the intensity versus time data. Used as an alternate name for the god Jupiter, JOVE is not an acronym but rather a call sign representing the area of the spectrum being studied. Radio-Skypipe is a free strip-chart program that takes the signal from the Radio JOVE receiver and digitizes it through the computer soundcard.

To begin collecting data, the coaxial cable is connected to the antenna on one end and directly connected to the Radio JOVE receiver, which takes the analog signal coming in from the antenna and amplifies it. The computer's sound card is used to digitize the signal. A speaker can also be hooked up to the receiver to hear the noise or "hissing" coming from the signal on the antenna. The JOVE receiver is then connected to a computer that is running the Radio-Skypipe software. Through calibration and tuning, the background noise can be mostly eliminated. Most of the solar bursts we observe are Type III solar bursts. Since these bursts occur very quickly, have a typical shape and have temperatures much higher than the background, it makes them easy to identify, as shown in Figure 9. Data was collected nearly every day from March 16, 2005 to August 31, 2007. The data was reduced by scanning and counting all the 20.1 MHz solar radio bursts for each day.

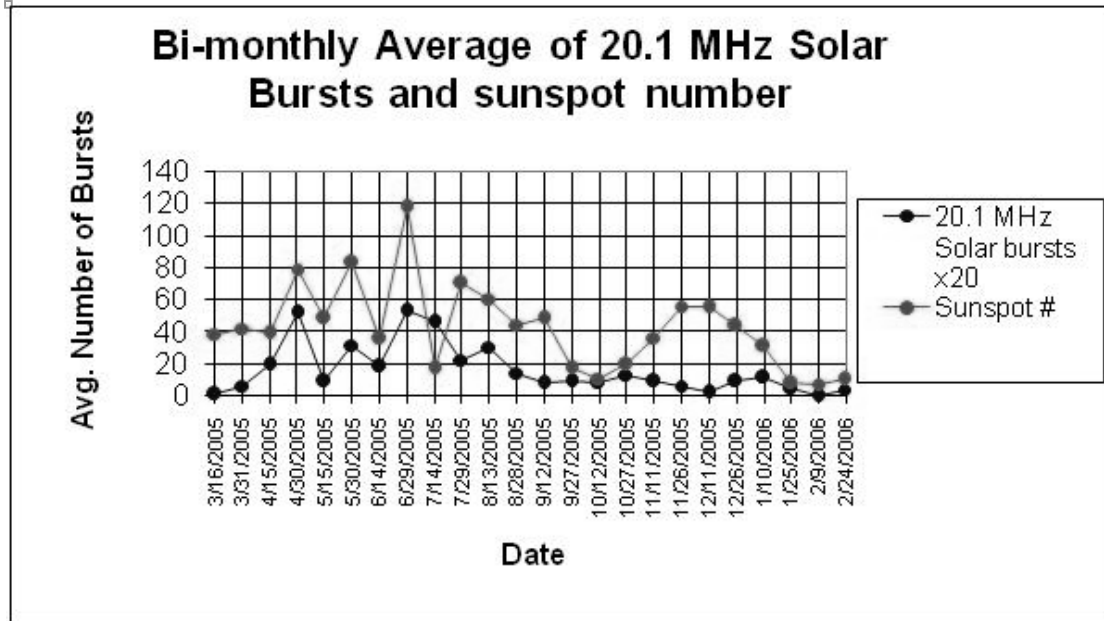


Fig. 9. Bi-monthly plot of average sunspot number vs. 20.1 MHz solar radio burst.

After going through all the data that we collected, as well as data we received from colleagues, we recorded the number of observed bursts, the number of radio bursts NOAA observed on that date, and the number of sunspots obtained from the space weather website (NOAA Space Weather Center, 2010). We multiplied our observed number of bursts per day by ten to make it easier to plot on a graph with sunspot number. The bi-monthly average number of 20.1 MHz bursts and sunspot number versus date were then graphed as shown in Figure 9, showing that the burst number generally increases when the number of sunspots increases and decreases when the sunspot number decreases. In Figure 10, trend lines were added using the midpoints between maxima and minima to show that both the burst number and sunspot number are decreasing over time. This is due to the fact that we are nearing the end of the solar minimum.

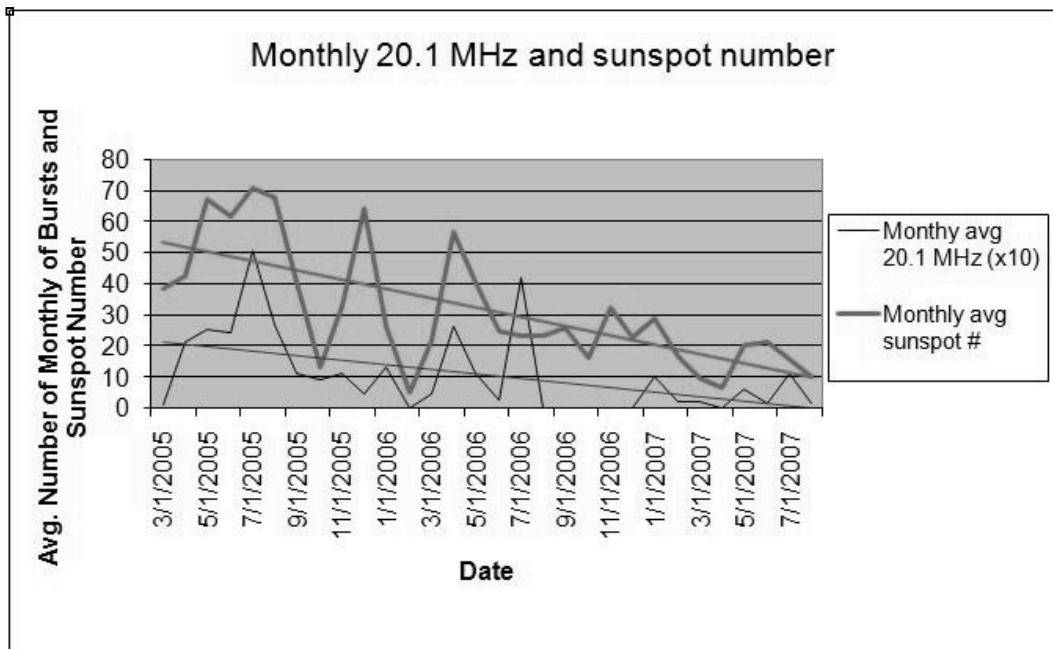


Fig. 10. Monthly plot of sunspot number and 20.1 MHz solar burst number over time.

From this we can see the downward trend in the number of sunspots over time. Also the increase in 20.1 MHz solar bursts in mid-2005 corresponds with an increase in the number of sunspot, and the decreases also correspond with developments later that year. There was little burst data in late 2005 and early 2006 which explains why there is not a corresponding increase in bursts along with the number of sunspots. We can see an increase of bursts in late 2006 that agree with the increase in sunspot number. There was little data collected in late 2006 and early 2007 due to equipment problems. When comparing our data with MSFC, we can see that our findings follow their data on sunspots at that time. Hathaway has done an extensive study on 2.8 GHz bursts, which are results of the synchrotron mechanism. Figure 11 shows the cyclic nature of the synchrotron mechanism and sunspot number.

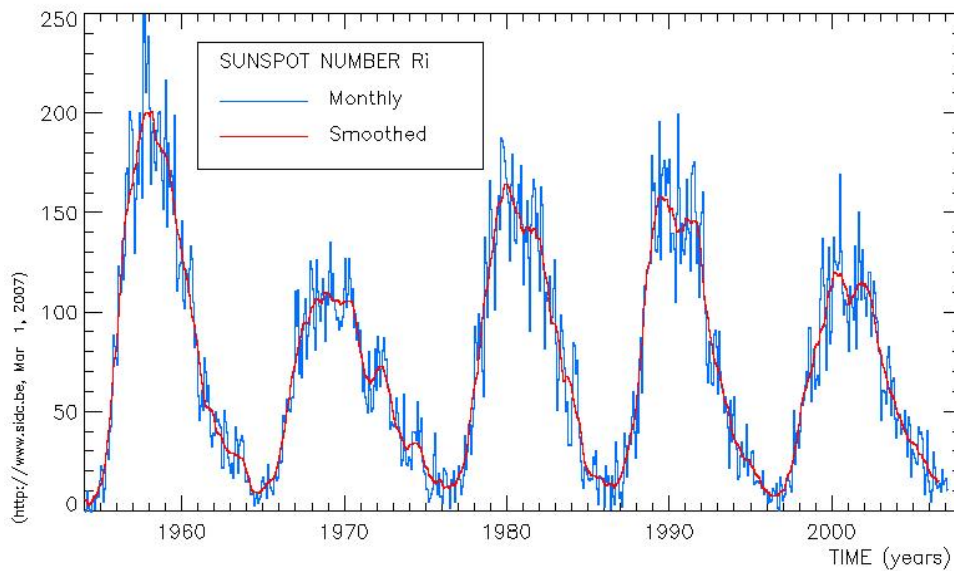
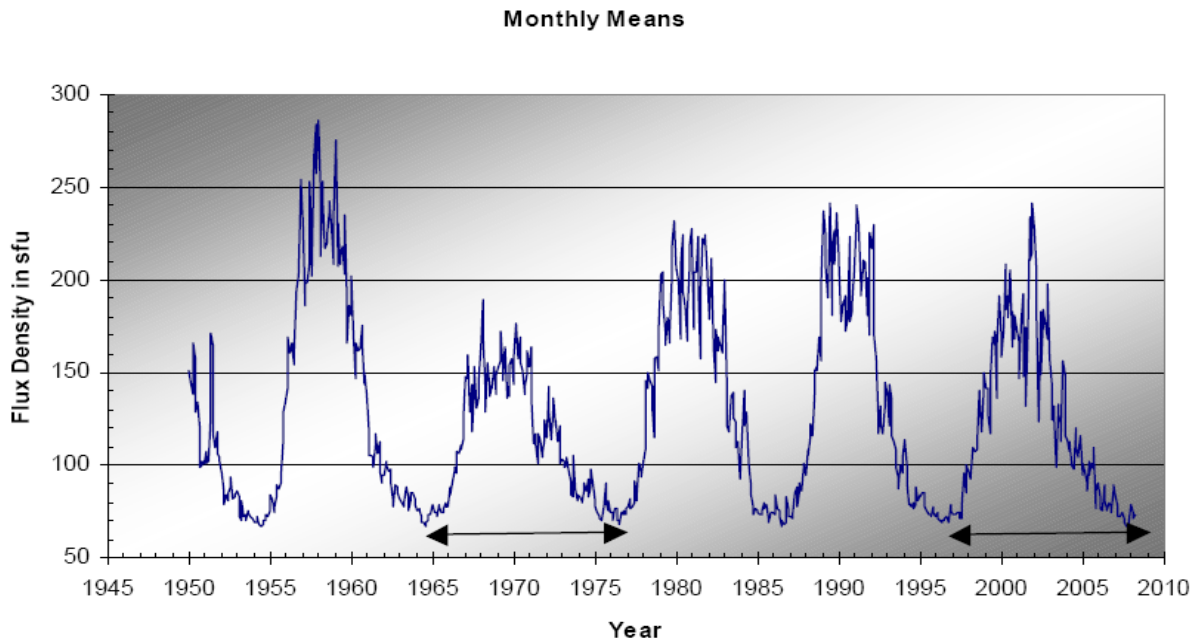


Fig. 11. Top: 2.8 GHz solar burst data from Hathaway; Bottom: sunspot number from Arizona..

From Figure 11, we see that there a connection exists between synchrotron emission and sunspot number. From 1955 to 1965 the flux density of the synchrotron maximum was about 270 solar flux units (sfu) [1 sfu = 1000 Jansky (Jy), and in SI units, $1 \text{ Jy} = 10^{-26} \frac{\text{W}}{\text{m}^2\text{Hz}}$]. From 1965 to 1975 the synchrotron maximum was curiously lower than the previous cycle by about 100 sfu. The sunspot cycle had a very similar change, and we deduced there must be something that ties

these two phenomena together. Theory predicts that to be the magnetic field. If there is a connection between solar synchrotron events and the number of sunspots, then it is safe to say that we should expect the same connection between solar cyclotron events and sunspots as well.

To show this statistically, the Pearson Product Moment Coefficient of Correlation method was used (Mendenhall; 1987). This procedure employs the “coefficient of correlation,” r , of the data set, where

$$r = \frac{SS_{xy}}{\sqrt{SS_x SS_y}}. \quad (23)$$

If the data had a perfect correlation, then $r = 1$; if there is no correlation at all then $r = 0$. SS denotes the sum of the squares of the desired variable:

$$SS_x = \sum_{i=1}^n x_i^2 - \frac{1}{n} (\sum_1^n x_i)^2 \quad (24)$$

$$SS_y = \sum_{i=1}^n y_i^2 - \frac{1}{n} (\sum_1^n y_i)^2 \quad (25)$$

$$SS_{xy} = \sum_{i=1}^n x_i^2 y_i^2 - \frac{1}{n} (\sum_1^n x_i)^2 (\sum_1^n y_i)^2. \quad (26)$$

The Pearson coefficient was applied to our sunspot data. Bi-monthly data on the sunspot number versus the 20.1 MHz solar burst data is plotted in Fig. 12 and an r value found comes out to be about 0.64, a positive correlation of 64%. Our short term (~ 2 years) low frequency data of Figure 12 shows good correlation with between the number of sunspots number and the synchrotron data.

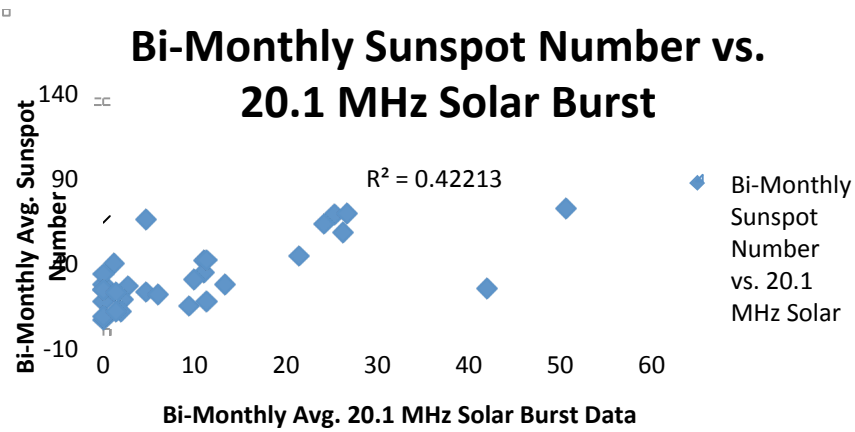


Fig. 12. Bi- monthly data of the sunspot number versus the 20.1 MHz solar burst data with r value of 0.64.

We then plotted given values of the number of sunspots and 20.1 MHz solar radio burst data for the same time period as shown in Figure 13. The r value gives us a correlation coefficient of approximately 0.93 or 93%.

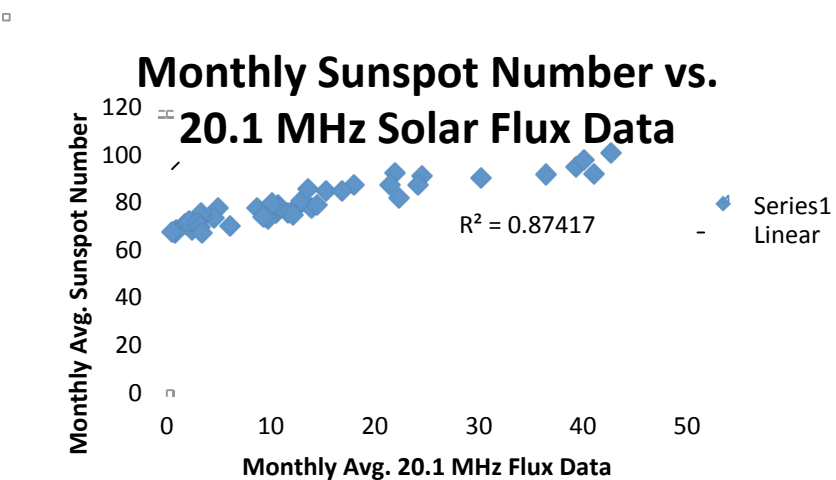


Fig. 13. Monthly average data of sunspot number versus 20.1 MHz solar burst data with r value of 0.93.

IV. Results

The data indicates that the 20.1 MHz solar burst data, which is a result of the classical cyclotron mechanism, shows a trend that follows the sunspot cycle. When comparing the 2.8 GHz solar burst data, a result of the relativistic synchrotron mechanism, to the sunspot data in Figure 13 from the same years, we can see that there is definitely a relationship. Since we know that the solar cyclotron and synchrotron mechanisms are a result of the same magnetic events, it should be expected that the 20.1 MHz solar bursts are related to the sunspot cycle. We found that the r value, the coefficient of correlation between the number of sunspots and 20.1 MHz solar radio bursts, was around 0.64, a positive correlation.

V. Conclusions

Radio astronomy has taught us that a strong correlation exists between the numbers of sunspots and solar burst activity, which was to be expected from theory. Our experiment involves a long-term monitoring of the Sun at a frequency of 20.1 MHz. This signal results from the cyclotron mechanism, which occurs when a charged particle travels at non-relativistic speeds along a magnetic field line, causing it to spiral and emit radiation. A 10.7 cm radiation results from the highly relativistic synchrotron mechanism. These energies are a result of extremely strong magnetic fields and fast-moving charged particles. The faster the particle moves, the narrower and focused the beam becomes. This narrowing of the beam is a result of the Lorentzian time dilation.

Data was taken of the number of solar bursts at 20.1 Mz, then plotted in daily, weekly, monthly, and bi-monthly graphs. The bi-monthly and monthly graphs showed the best trends. More sunspot data dating back to 2000 was added to the monthly data to confirm a downward trend due to the ending of the solar minimum. These graphs were then compared to a graph of the sunspot number to show that our downward trend is close to the solar data from Marshall Space Flight Center. Our data shows a positive correlation of approximately 65%. Our data was then compared to graphs of 2.8 GHz solar burst data (from the synchrotron mechanism) and overall number of sunspots. Both solar burst activity and sunspot activity show a long term cyclic behavior. It then stands to reason that solar burst activity at a different frequency should be the same. Also if such positive trends can be shown during a time of very little data (tail end of solar minimum), the relationship between solar radio bursts and sunspot number should become more obvious as we approach the solar maximum.

VI. References

1. Bellan, Paul M. "Alfvén-Wave Instability of Current Sheets in Force-Free Collisionless Plasmas," *Phys. Rev. Lett.* **83**, 4768-771 (1999).
2. Condon, J.J., and S.M. Ransom. "Essential Radio Astronomy," *National Radio Astronomy Observatory, Charlottesville*. 22 Oct. 2008, 26 Jan. 2010, <<http://www.cv.nrao.edu/course/astr534/ERA.shtml>>.
3. Flagg, Richard S. *Listening to Jupiter: A Guide for the Radio Astronomer* 2nd ed., Radio-Sky, 2005.
4. Freedman, Roger, and William J. Kaufmann. *Universe: The Solar System*, 2nd ed., W. H. Freeman, New York, NY, 2005.
5. Gary, Dale E., and Christoph U. Keller. *Solar and Space Weather Radiophysics Current Status and Future Developments*, 2nd ed., Springer, New York, NY, 2004.
6. Kraus, John Daniel. *Radio Astronomy*. 2nd ed., Cygnus-Quasar, Powell, OH, 1986.
7. Melia, Fulvio. *Electrodynamics*. Chicago, IL, Univ. of Chicago Press, Chicago, IL, 2001.
8. Melia, Fulvio. *High-energy Astrophysics*. Princeton Univ. Press, Princeton NJ, 2009.
9. Mendenhall, William. *Introduction to Probability and Statistics*, 7th ed. PWS, Boston, MA, 1987.
10. Priest, Eric Ronald, and Terry G. Forbes. *Magnetic Reconnection: MHD Theory and Applications*. Cambridge Univ. Press, Cambridge, UK, 2006.

11. "Solar Cycle Progression and Prediction." *NOAA / NWS Space Weather Prediction Center*. 5 Jan. 2010. Web. 22 Jan. 2010. <<http://www.swpc.noaa.gov/SolarCycle/>>.
12. "Index of /ftplib/indices/old_indices." *NOAA / NWS Space Weather Prediction Center*. Web. 22 Jan. 2010. <http://www.swpc.noaa.gov/ftplib/indices/old_indices/>.
13. J.D. Jackson, *Classical Electrodynamics*, John Wiley & Sons, New York, NY, 1975.

Method for Extracting the Frequency Response of an Audio System from a Recording

Herman Orgeron

Abstract. The ability to compare the technical performance of audio systems is necessary to choose the microphone system that best meets operational requirements. A common method to evaluate a system's performance is to generate a transfer function for the system and determine the frequency response. Normally this is done by connecting the system to a network analyzer, however not all systems have this ability. This paper outlines procedures developed to non-traditionally measure the frequency response of audio systems using recorded data files.

INTRODUCTION

There are a variety of systems used to record and transmit audio signals. Each system has its own advantages and disadvantages, typically trading off cost, size, and power consumption for audio fidelity. In order to select the right system for a given situation, it is desirable to use unbiased indicators of performance to determine which system has the best audio quality for a given set of circumstances.

Therefore, it is necessary to develop a simple method to quantify and compare systems that operate in vastly different ways. One of the best ways of quantifying audio quality is to measure a system's frequency response—a gauge of a system's output spectrum given a specific input. The frequency response is used to graphically display how the recording system changes or distorts the input audio signal. The most desirable result is that the plot of the frequency response is a nearly flat line, meaning that at any given frequency the system's response to the input signal is constant.

Historically, an audio system's frequency response was determined by placing the microphone in an anechoic chamber and sweeping through the audio spectrum with a well defined noise source, i.e. a loudspeaker. The system output would then be connected to a network analyzer which would display its response across the desired audio spectrum. This technique is not available to digital systems that record audio for later review—there is no connection to allow audio to be fed into an analyzer. The lack of a real time analog audio stream prevents the use of traditional network analyzers and associated procedures. This complicates extracting the frequency response of the system and must be taken into account when developing a test methodology.

I. APPROACH

The method presented in this paper is designed to generate the frequency response for systems that do not produce continuous audio output—instead they save the audio data into packets or files and all of the analysis must be done post-process. This method utilizes data acquisition and processing programs—in this instance MATLAB was used due to availability—and computer data acquisition cards to acquire the audio from multiple systems and to process the system frequency response.

The basis for this method is that if two systems, one whose properties are known, and one whose properties are unknown, are exposed to the same audio environment, the unknown system's response can be determined based on the known system's response.

In order to determine the frequency response of a particular system, the Power Spectral Density (PSD) of the saved recording is taken. The PSD plots acoustic power (dB) against a specific frequency spectrum (Hz). By comparing two systems with the same inputs, any differences in the PSDs is a difference in the systems.

In this case, a system is defined as anything that takes an input signal, operates on it, and produces an output signal.

$$x(t) \rightarrow \text{System } h(t) \rightarrow y(t)$$

The transfer response for the system is $h(t)$ and the output defined in the time domain is

$$y(t) = x(t) * h(t) \quad (1)$$

where $*$ is the convolution operator¹ and is defined as

$$(f * g)(t) = \int f(\tau)g(t-\tau)d\tau. \quad (2)$$

Convolution is used to mathematically describe the interaction between two signals and how they produce a third, different signal. Typically the third signal created by using the convolution operator is a modified version of one of the original signals.

The convolution theorem can be used to simplify equation (1) by converting it from the time to the frequency domain. The convolution theorem states that the Fourier transform of two convoluted signals is equal to the Fourier transform of each signal multiplied together,

$$F[f * g] = F[f] \cdot F[g] \quad (3)$$

where F denotes a Fourier transform operator². Fourier transforming $x(t)$ and $h(t)$ converts the signals from the time domain, (t) , into the frequency domain, (ω) . Thus, equation (1) is simplified from a convolution of signals at a given time to a product of signals at a given frequency:

$$y(\omega) = x(\omega) \cdot h(\omega). \quad (4)$$

The raw data being fed into the system from the respective microphones is in volts and needs to be converted into a decibel scale, a measure of loudness, using the identity

$$L_{dB} = 10 \log_{10}(A_1^2/A_0^2), \quad (5)$$

where L_{dB} is the ratio of A_1 to A_0 in decibels, A_1 is the measured amplitude, and A_0 is the reference amplitude³. In this case, the reference amplitude is 1 V. Equation (5) can be applied to the $x(\omega)$ and $h(\omega)$ signals from equation (4), along with the general multiplicative logarithm identity,

$$\log(x \cdot y) = \log(x) + \log(y), \quad (6)$$

to simplify equation (1) into vector addition, where $x(\omega)$ and $h(\omega)$ are signals in the frequency domain with the units of decibels. The frequency equation is now represented by

$$\log(y(\omega)) = \log(x(\omega)) + \log(h(\omega)). \quad (7)$$

The general form to calculate the frequency response for the unknown system based on the known system's input can be written as a system of equations:

$$\log(y_k(\omega)) = \log(x(\omega)) + \log(h_k(\omega)) \quad (8)$$

$$\log(y_u(\omega)) = \log(x(\omega)) + \log(h_u(\omega)) \quad (9)$$

where

$y_k(\omega)$ is the measured PSD of the known system,
 $y_u(\omega)$ is the measured PSD of the unknown system,
 $h_k(\omega)$ is the transfer response of the known system,
 $h_u(\omega)$ is the transfer response of the unknown system,
and $x(\omega)$ is the sound pressure level in the anechoic test chamber.

The unknown transfer response, $h_u(\omega)$, can be determined by solving equation (8) for $x(\omega)$ and substituting into equation (9), resulting in

$$\log(y_u(\omega)) = \log(y_k(\omega)) - \log(h_k(\omega)) + \log(h_u(\omega)). \quad (10)$$

We can now determine $h_u(\omega)$ as a function of the two measurements, $y_k(\omega)$ and $y_u(\omega)$, and the given transfer response, $h_k(\omega)$:

$$\log(h_u(\omega)) = \log(y_u(\omega)) - [\log(y_k(\omega)) - \log(h_k(\omega))] \quad (11)$$

Expression (11) can be simplified down into its final form,

$$h_u(\omega) = [y_u(\omega) \cdot h_k(\omega)] / y_k(\omega) \quad (12)$$

using logarithmic identities and then taking the inverse logarithm of both sides of the equation.

The transfer response of the unknown system is determined by subtracting the test chamber sound pressure level from the measured system response. The sound pressure level in the test chamber is determined using the measured response of the known system, from here on referred to as the reference microphone, and the published frequency response taken from the manufacturer's specifications. The final accuracy of the transfer response for the unknown system, from here out referred to as the System Under Test (SUT), depends on the accuracy of the reference microphone, so only high quality laboratory microphone systems should be used.

II. EXPERIMENTAL PROCEDURE

In order to acoustically isolate the systems, all measurements were made using a Brüel & Kjør Type 4232 Portable Anechoic Chamber⁴. The reference microphone and the microphone for the SUT were placed inside the chamber. Using the chamber's internal loudspeaker, a frequency sweep, or 'chirp' was played. The chirp spanned from 500 to 5000 Hz and lasted 5 seconds. This was repeated with one second of silence

between each sweep. The chirp was generated using Sound Forge, a computer software program designed for digital audio editing. The digital signal was then converted into analog via computer sound card and output to a loudspeaker. A sound card with a flat frequency response is necessary to avoid distorting the signal and changing the results. Based on this requirement, an Echo Gina 3G card⁵ was used.

The reference microphone was an ACO Pacific Type 7012 microphone⁶, paired with a matched preamplifier, which was already calibrated. Its manufacturer-provided frequency response is extremely flat from 10 to 10000 Hz (Fig 1), making it a good reference choice. The output of the reference microphone was recorded using a Tektronix TDS6804B Digital Oscilloscope. The SUT audio was recorded using the equipment and software provided with the system. Both recordings were then transferred into MATLAB for post-processing (Fig 2).

This test method was used to compare three audio systems. The first system tested was another microphone with a known frequency response (Tibbetts Model 251-01). If the methodology was accurate, the transfer response generated would be the same as (or within a reasonable error to) the theoretical frequency response published for the microphone.

The second SUT was a digital proprietary wireless microphone. This system used a microphone connected to a wireless radio frequency (RF) transmitter. The data from the microphone was digitized and transmitted to a receiver attached to a computer. Software included with the system captured the signal and recorded the audio.

The final system tested was a wireless microphone system which communicated using a cellular network, GSM (Global System for Mobile communications). The system used Bluetooth to transmit the audio signal from the microphone to a base unit. The base unit then sent the signal over the cellular network to a computer in order to be recorded.

Both the RF and the GSM cellular systems provided true unknowns to test this method because there is no frequency response data published for either system, and neither provides a real-time audio stream for measurements using conventional audio test equipment.

Audio recordings of the chirp were made simultaneously in the chamber with the SUT and reference microphone and saved as .wav files. The data taken from the RF and GSM systems was done using the best-case scenario—short range transmission with no interfering obstacles. A MATLAB program was written to process the data and to calculate the frequency responses of the systems.

In MATLAB the two time domain data sets from each system were cut to the same size, approximately six seconds—the length of the full sweep including silence in the beginning and the end. Then the PSD via periodogram was taken for each data set.

The normalized PSD for the reference microphone, $y_k(\omega)$, was then subtracted from the published frequency response, $h_k(\omega)$. This provides a measure of the audio signal that is present in the chamber at the input of the SUT. With the input known, the SUT transfer response could then be determined by subtracting the SUT measured response from the input, $x(\omega)$.

III. RESULTS

The results from the tests were very promising. The Tibbetts microphone performed closely to its published data⁷ (Fig 3). The published frequency response variance from unit to unit for the microphone was ± 3 dB. The absolute difference between the frequency response measured using this technique and the published response was less than 6 dB at all frequencies.

The digital wireless microphone displayed an almost perfectly flat frequency response graph. The GSM system did not perform as well, displaying a very broken, choppy curve (Fig 4).

These results were further verified by plotting the time domain audio data received from each of the units (Fig 5). The plots for the Tibbetts microphone and the digital wireless microphone are both very smooth, where the GSM plot is very distorted.

The poor response from the GSM system is most likely due to the way that the cellular network transmits the data. The data is compressed for efficiency using adaptive codecs before sending it through the network. Unfortunately, the codecs can result in the loss of audio quality, especially if there is not a high signal to noise ratio.

IV. CONCLUSION

The experimental method described has proven to be a useful tool for evaluating and comparing audio systems. The accuracy of the technique was validated on a known system before being used to test two unknown systems. The response output from the two unknown systems was validated by comparing the frequency response to their audio output—as expected, the system that output smooth audio had a far better response than the system that produced choppy audio.

This method provides a good comparison because it does not just account for the acoustic capabilities of a recording device, but the entire system, including losses from other causes such as encoding and transmission.

The next step for this method would be to fine tune it so that it would be able to extract an averaged frequency response from any common, broad-spectrum audio source, i.e. a voice recording or white noise. This would add robustness to system testing where the operator would not need the system to be physically present, just data that it had recorded. Additionally, the frequency responses generated from this method could be used to correct recorded signals from these systems in post-processing.

V. ACKNOWLEDGEMENTS

Every paper gains from the critical comments of its author's friends and colleagues. I would like to thank in particular Mr. John Latess, without whose guidance this project would never have been realized.

VI. REFERENCES

1. Weisstein, E. W. (n.d.). Convolution. *MathWorld—A Wolfram Web Resource*. Retrieved on October 13, 2009 from <http://mathworld.wolfram.com/Convolution.html>

2. Weisstein, E. W. (n.d.). Convolution theorem. *MathWorld—A Wolfram Web Resource*. Retrieved on October 13, 2009 from <http://mathworld.wolfram.com/ConvolutionTheorem.html>
3. Everest, F. A. (2001). *Master handbook of acoustics, Fourth edition*. New York: McGraw-Hill.
4. *Product data: Anechoic Test Box – Type 4232*. (2005). Brüel & Kjær. Retrieved on November 28, 2008 from <http://www.bruel.ru/UserFiles/File.4232.pdf>
5. *Layla 3G/Gina 3G owner's manual version 1.0.1 for Windows*. (2007, April 23). Echo Audio. Retrieved on November 26, 2008 from <http://echoaudio.com/Downloads/Manuals/Echo3G%20Windows%20Manual%201.0.1.pdf>
6. *Precision microphones and systems for end users and OEM*. (2002). Aco Pacific. Retrieved on December 1, 2008 from <http://www.acopacific.com/acopacat.pdf>
7. *Microphone products 251 Series technical data sheet*. (2004). Tibbetts Industries. Retrieved on November 28, 2008 from <http://www.tibbettsindustries.com/pdf/108257224.pdf>

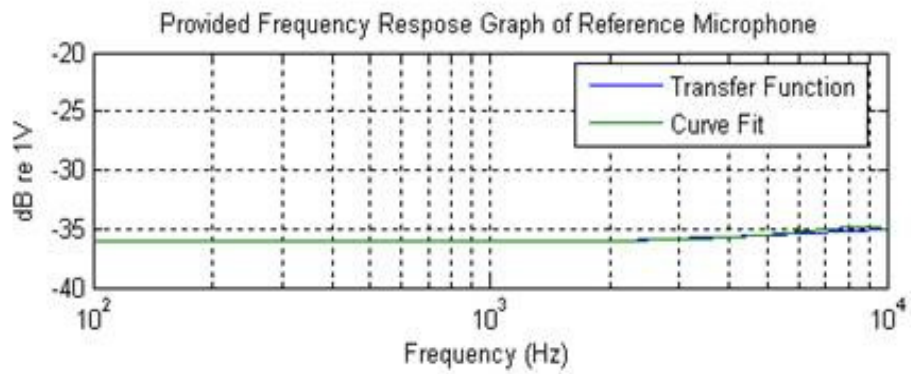


(Fig 1) Theoretical frequency response graph for the reference microphone and the MATLAB curve fit, from 100 to 10000 Hz

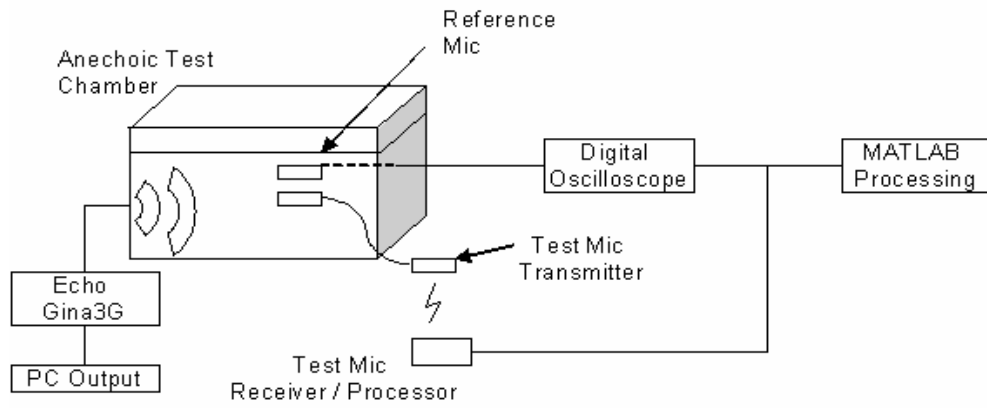


(Fig 2) Diagram of experiment set-up.

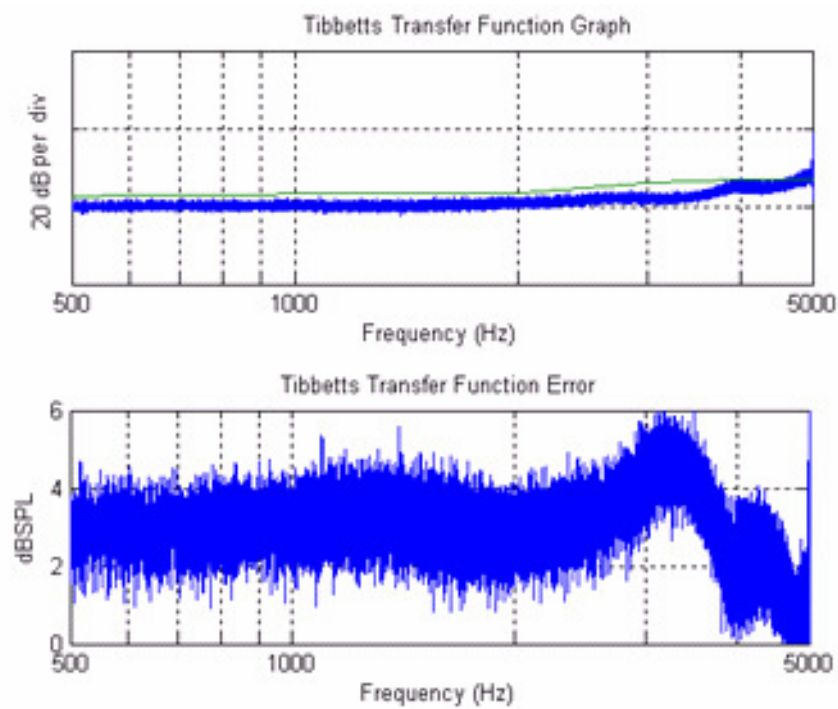


(Fig 3) Above: Graph of Tibbetts transfer function (blue) and published theoretical transfer (green). Below: Graph of the absolute error between the experimental and theoretical.

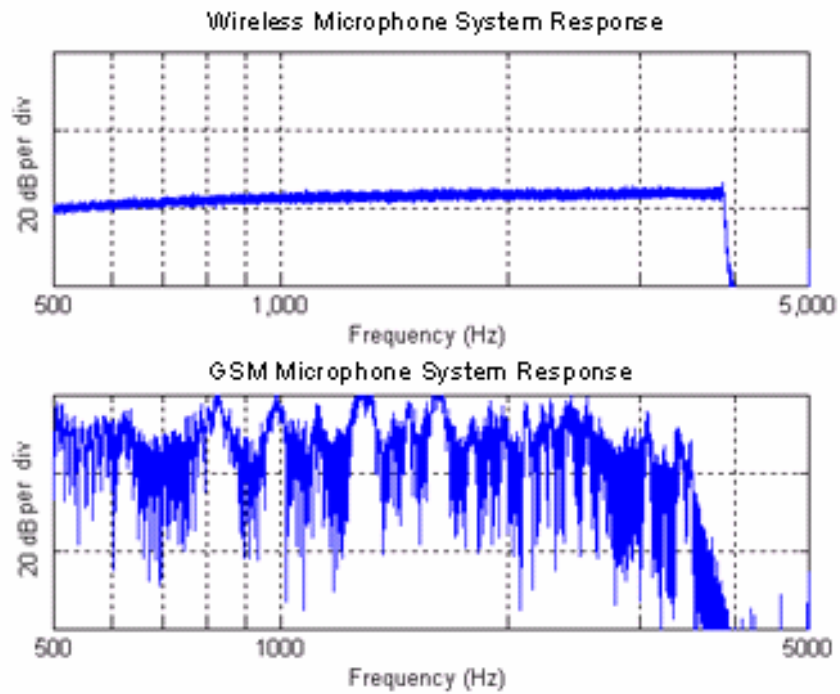


(Fig 4) Above: Frequency response for the wireless microphone. Below: Frequency response for the GSM based microphone.

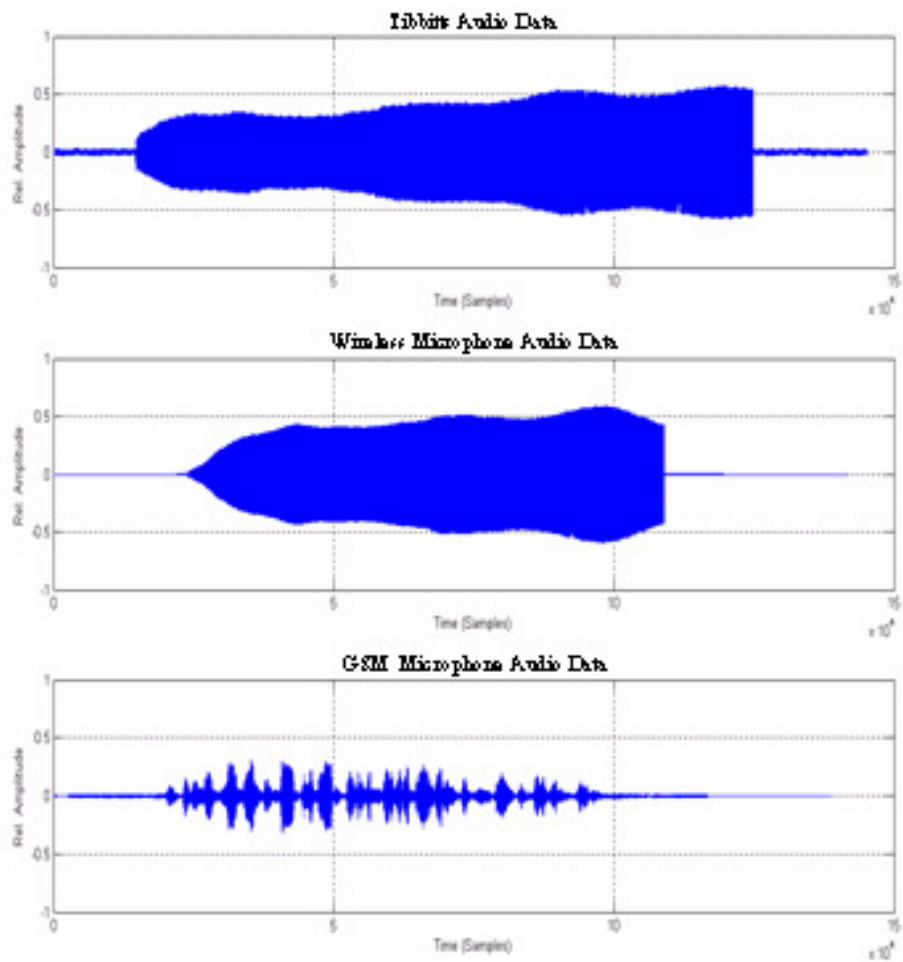


(Fig 5) Top: Tibbitts audio data. Middle: Wireless microphone audio data. Bottom: GSM microphone audio data.